Highly Oriented Nanowire Thin Films with Anisotropic Optical Properties Driven by the Simultaneous Influence of Surface Templating and Shear Forces

Patrick T. Probst, Sribharani Sekar, Tobias A. F. König, Petr Formanek, Gero Decher, Andreas Fery, Matthias Pauly

Highly oriented nanowire thin films with anisotropic optical properties driven by the simultaneous influence of surface templating and shear forces

*Patrick T. Probst,[‡1] Sribharani Sekar,[‡1,2] Tobias A.F. König,[*1,3] Petr Formanek,[1] Gero Decher,[*2] Andreas Fery,[*1,3,4] and Matthias Pauly[*2]*

1. Leibniz-Institut für Polymerforschung Dresden e.V., Institute of Physical Chemistry and Polymer Physics, Hohe Str. 6, D-01069 Dresden, Germany

2. Université de Strasbourg, CNRS, Institut Charles Sadron, F-67000 Strasbourg, France

3. Cluster of Excellence Centre for Advancing Electronics Dresden (CFAED), Technische Universität Dresden, D-01062 Dresden, Germany

4. Department of Physical Chemistry of Polymeric Materials, Technische Universität Dresden, Hohe Str. 6, D-01069 Dresden, Germany

KEYWORDS : nanowire, wrinkles, spray coating, oriented assembly, thin films, anisotropic optical properties

ABSTRACT

The functional properties of nanoparticle thin films depend strongly on the arrangement of the nanoparticles within the material. In particular, anisotropic opto-electronic properties can be achieved through the aligned assembly of 1D-nanomaterials such as silver nanowires (AgNWs). However, the control of the hierarchical organization of these nanoscale building blocks across multiple length scales and over large areas is still a challenge. Here, we show that the oriented deposition of AgNWs using Grazing Incidence Spraying of the nano-object suspensions on a substrate comprising parallel surface wrinkles readily produces highly oriented monolayer thin films on macroscopic areas (>5 × 5 mm^2). The use of textured substrates enhances the degree of ordering as compared to flat ones and increases the area over which AgNWs are oriented. The resulting microscopic linear arrangement of AgNWs evaluated by scanning electron microscopy (SEM) reflects in a pronounced macroscopic optical anisotropy measured by conventional polarized UV-Vis-NIR spectroscopy. The enhanced ordering obtained when spraying is done in the same direction as the wrinkles makes this approach more robust against small rotational offsets during preparation. On the contrary, the templating effect of the wrinkle topography can even dominate the shear-driven alignment when spraying is performed perpendicular to the wrinkles: the concomitant but opposing influence of topographic confinement (alignment along the wrinkles) and of spray-induced shear forces (orientation along the spraying direction) lead to films in which the predominant orientation of AgNWs gradually changes from one direction to its perpendicular one over the same substrate in a single processing step. This demonstrates that exploiting the subtle balance between shear forces and substrate-nanowire interactions mediated by wrinkles offers a new way to control the self-assembly of nanoparticles into more complex patterns.

Introduction

Oriented nanomaterials and thin films with anisotropic opto-electronic properties are currently widely investigated because of their numerous potential applications in fields as diverse as flexible electronics,[1,2] photovoltaics,[3,4] polarization optics,[5,6] sensing[7,8] and metamaterials.[9,10] The opto-electronic properties in such assemblies strongly depend on the arrangement of the nano-objects within the material.[11,12] This is particularly true for optical metamaterials, whose properties arise from the subwavelength nanostructure (unit cell) rather than from its constituent materials.[9,10,13] The controlled positioning of these repeating unit cells allows engineering the far-field optical properties, and the metamaterial transmittance, absorbance and reflectance. The collective response does not derive only from the bulk properties of the base materials, but rather from the shape, size, orientation and arrangement of the individual building blocks.[14-16] In particular, plasmonic metasurfaces[17,18] consist of an array of subwavelength anisotropic light scatterers (e.g. plasmonic resonators such as metallic nano-antennas).[10,19,20]

Most of these metasurfaces are fabricated by top-down methods like direct laser writing[21,22] or e-beam lithography.[23,24] However, these techniques have the disadvantage of being quite expensive and slow, and the required subwavelength dimensions (i.e. in the range of tens of nm for optical applications) push these conventional techniques to their limit. Moreover, lithographically-produced plasmonic arrays usually suffer from polycrystallinity and rough surfaces of the metallic features, which introduces unfavorable plasmonic damping. Self-assembly of wet-chemically synthesized, well-defined plasmonic building blocks appears to be a promising alternative that is capable of large-scale production.[15,25-33] As metasurfaces are composed of buildings blocks that must contain a certain anisotropy, plasmonic nanowires and nanorods have become a starting material of choice for many self-assembled plasmonic

metamaterials.[10,34-36] However, the hierarchical organization of these nanoscale building blocks into two- or three-dimensional nanostructures with well-controlled location, orientation, and spacing across multiple length scales is still a challenge. Several approaches for the assembly of (plasmonic) nanowires and nanorods in thin films with in-plane anisotropy have been developed,[37-39] including Langmuir-Blodgett[40,41] or the use of external electrical or magnetic fields.[42-44] Other techniques use flow-induced shear in fluidic cells,[45] in a capillary[7,46] or by evaporating spray droplets onto hot surfaces.[47] However, these methods are limited in their ability to yield uniformly aligned films over large areas and they are restricted to small groups of components.

Most of these approaches rely on the control of capillary forces and interfacial flows upon evaporation of the nano-object suspension. Chemically or topographically structured substrates can be used to introduce an additional level of hierarchy. Surface corrugations lead to a local modification of the capillary forces and thus control the pattern of nanoparticles formed during the solvent evaporation. Such wrinkled substrates have been successfully used over the last years,[48] in particular by Fery and coworkers,[49-52] to form highly oriented assemblies of gold nanoparticles and gold nanorods over macroscopic areas. Wrinkle formation in stiff thin films on compliant substrates results from mechanical instabilities upon compression,[53-56] and the templates can thus be of macroscopic dimensions. Nevertheless, they comprise (sub-)micron features of tunable size. This makes them attractive as templates for scalable bottom-up colloidal self-assembly to create functional materials.

Recently, Pauly, Decher and coworkers have introduced Grazing Incidence Spraying (GIS)[57-59] as a novel assembly method that relies on the low-angle spraying of a suspension of nanorod/nanowire on a substrate. Using this approach, monolayer thin films of gold nanorods,[57]

silver nanowires[57,58] or cellulose microfibrils[59] in which all the nano-objects are pointing in the same in-plane direction over >cm^2 areas can be obtained. They have also shown[58] that it is possible to build oriented multilayer thin films of controlled thickness by combining GIS with Layer-by-Layer (LbL) assembly.[60-63]

In this paper, we apply the GIS oriented assembly approach on wrinkle-structured receiver substrates to further improve the uniaxial alignment of AgNWs and investigate the effect of the surface topography on the robustness of shear-driven orientation. The corrugations seem to direct the flow of the nanowire suspension such that the area over which AgNWs are highly aligned can be significantly increased when spraying is applied along the wrinkle direction. Surprisingly, when the macroscopic flow is directed perpendicular to the wrinkles, under certain conditions, the orientation direction is governed by the corrugations rather than by the spraying direction. This alignment of nano-objects on large areas results in a macroscopic anisotropy in the optical properties as probed by polarized UV-Vis-NIR spectroscopy. GIS is a technique that works for a broad range of 1D-nanomaterials (metals, semi-conductors, carbon-based material,…) and can be implemented on a continuous production line. As wrinkled substrates are compatible with roll-to-roll manufacturing,[64] the proposed approach is a step towards the large-scale production of versatile anisotropic thin films that can be used for instance as plasmonic metasurfaces, dichroic optical coatings or transparent conducting layers, or integrated in more complex devices such as solar cells[3,39] or polarization-dependent photodetectors.[65,66]

Results and Discussion

In order to investigate the effect of parallel wrinkles on the quality of linear ordering, AgNWs (diameter: 47 ± 6 nm, length: 4.2 ± 1.5 μm) have been deposited on a wrinkled polydimethylsiloxane (PDMS) substrate using GIS with spraying applied along the wrinkle

direction ($\varphi = 0°$) and compared to a flat receiver substrate (Figure 1). The only difference between those two substrates is that a given uni-axial strain ($\Delta L/L_0 = 30–40\%$) has been applied to one substrate during the plasma-induced oxidation of PDMS, leading to a surface that is homogeneously wrinkled over large areas after relaxation. These two samples are thus chemically equivalent, as they both consist of surface-oxidized PDMS coated by poly(ethyleneimine) (PEI), and they only differ in terms of their surface topography: as shown by Atomic Force Microscopy (AFM, Fig. S1 in the Supporting Information), the so-called "flat" substrate has a low surface roughness (rms = 0.6 nm after PEI coating), whereas the wrinkled substrates have a corrugated surface that shows a sinusoidal profile with an average wavelength of 950 ± 20 nm and amplitude of 130 ± 10 nm. The lateral extension of the PDMS substrate upon relaxation (Poisson's effect) causes cracks in the brittle oxide layer that are oriented perpendicular to the wrinkles.

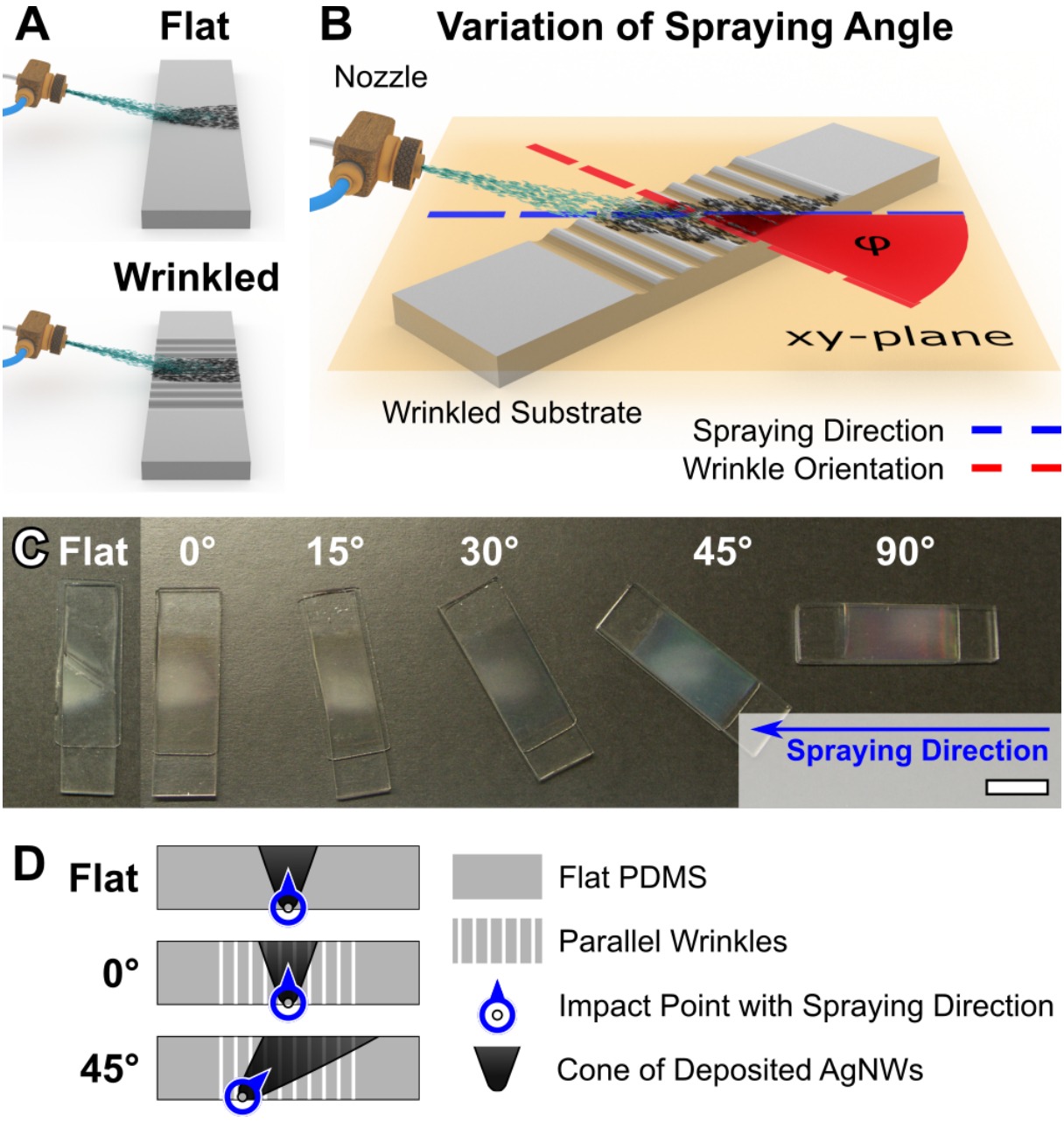

Figure 1. *Schematic representation of the Grazing Incidence Spraying (GIS) experiments. (A) Comparison between spraying a silver nanowire (AgNW) suspension onto a flat receiver substrate (top) and a corrugated ("wrinkled") one (bottom). (B) The wrinkle-assisted linear alignment was evaluated by a controlled variation of the in-plane (xy-plane) spraying angle* φ *defined as the angle between the wrinkle direction (red dashed line) and the projection of the*

spraying direction on the substrate plane (blue dashed line). The spraying nozzle is kept at a constant distance of 1 cm above the substrate and the spray axis forms an angle of 15° with the substrate plane. (C) Photographs of samples obtained with various spraying angles φ starting from 0° (spraying parallel to the wrinkles) and ending at 90° (perpendicular to the wrinkles). The AgNW coating appears as a homogeneous grayish film, whereas the refracted colors arise from the periodic structure of the corrugated surface. Scale bar: 1 cm. (D) schematic top-view representation of flat and wrinkled substrates highlighting the position of the impact of the spray jet on the surface, the spraying direction (with respect to the wrinkle direction when applicable) and the shape of the coated area.

The spraying of AgNWs on both the flat and the wrinkled PEI-coated PDMS substrate results in a ~1 cm^2 grayish film. The macroscopic parabolic shape of the film results from the intersection of the spray cone and the substrate planar interface (Figure 1C).

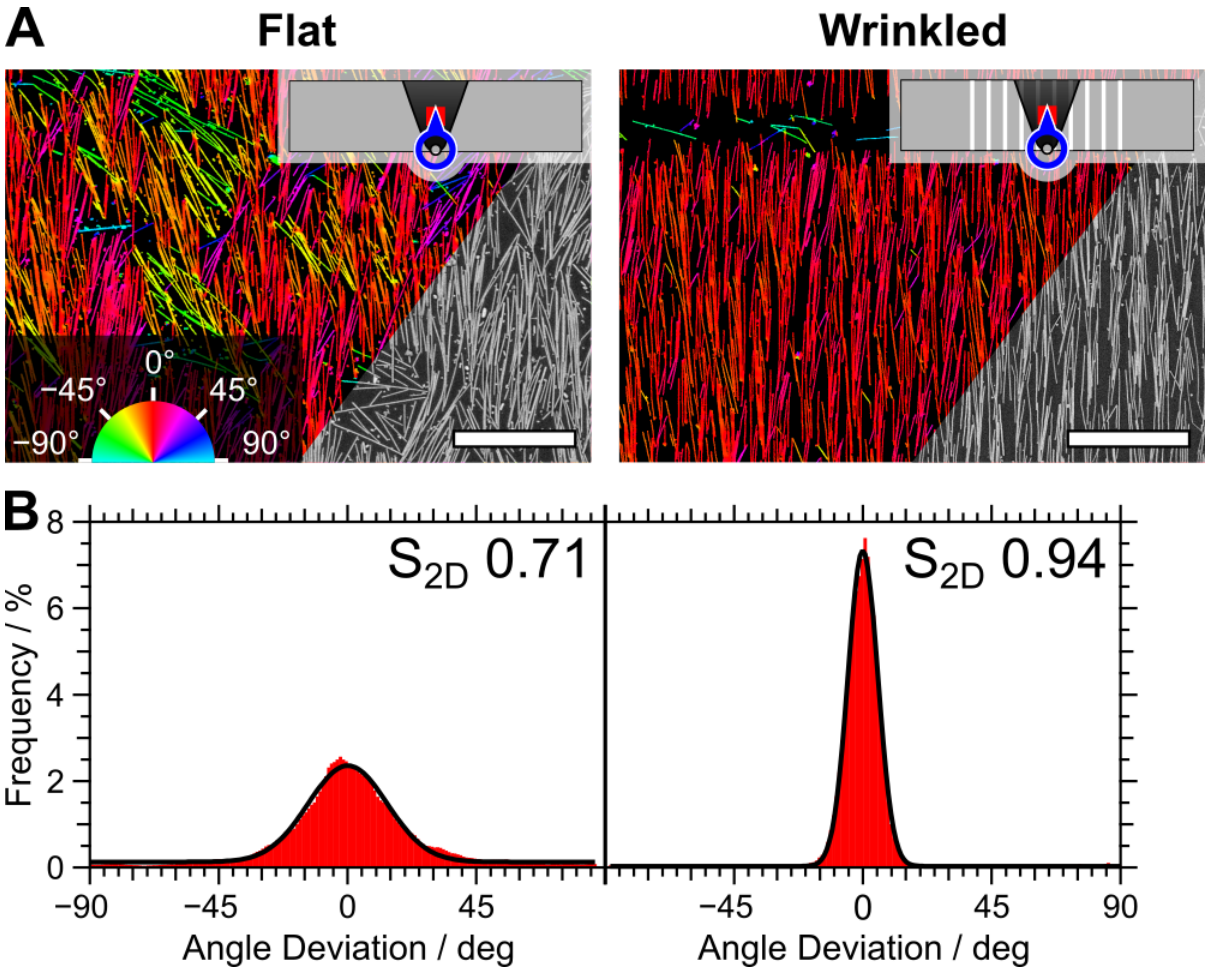

Figure 2. *Comparison between the flat and wrinkled substrates after GIS of AgNWs. (A) The SEM images are analyzed in order to determine the AgNW orientation for the flat (left) and wrinkled substrates (right). The SEM images are split into the original image (bottom right part of each image) and an orientation-highlighted image in which the wires are color-coded according to their orientation (the color scale is shown as an inset). The position at which the images have been taken is highlighted with a red square on the schematic of the samples (inset). The scale bar is 5 μm. (B) The distribution of angle deviation from the reference direction is extracted from the SEM image analysis and is quantified by the 2D order parameter S_{2D} (see also equation 1).*

Figure 2A clearly shows that GIS assembly of AgNWs leads to a thin film consisting of a monolayer of oriented AgNWs on both the flat and corrugated PDMS substrates. Repulsive particle-particle interaction of the charged alike polyvinylpyrrolidone-coated AgNWs (zeta-potential ≈ -30 mV) prevents the formation of multilayers and the particles oriented by shear forces are immobilized on the positively charged PEI-functionalized surface due to electrostatic interactions. The SEM images of the thin films reveal that AgNWs are deposited as a side-by-side oriented monolayer with a predominant orientation but no positional order. Consequently, the structure can be described as 2D nematic. It appears also that the quality of ordering is higher on the corrugated PDMS substrate compared to the flat substrate, which can be explained by the combined effect of the confinement of the flow at the solid-liquid interface offered by the 1D topography and the intrinsic tendency of nanowires and nanorods to orient along the wrinkles to maximize their interaction with the substrate. Whereas on the flat substrate side-by-side alignment of AgNWs occurs only in domains which are a few tens of μm^2 in size, parallel corrugations facilitate linear alignment over large areas. The consequently more effective packing of particles allows for larger coverage on the wrinkled sample (88% on wrinkles vs. 79% on the flat substrate). In order to quantify the degree of ordering, the SEM images have been analyzed using OrientationJ,[67] a plugin for ImageJ,[68,69] which is based on the analysis of the gray-level in a local neighborhood. The full image treatment procedure is detailed in Fig. S2. The local orientation angle α is determined for each pixel of the SEM image and color-coded according to the depicted color legend (inset of Figure 2A). In the resulting false-color images, nanowires oriented along the vertical direction ($\alpha = 0°$) appear in red whereas the nanowires aligned along the horizontal direction ($\alpha = \pm 90°$) are in light blue (see also Fig. S3).

The distribution of orientation angle α can thus be measured over the entire SEM image. This distribution has a Gaussian shape with its maximum defining the angle of predominant orientation α_{max} which coincides with the spraying direction for the flat substrate and to the wrinkle direction for the corrugated one. The deviation from this predominant direction, defined as $\alpha - \alpha_{max}$, is relevant for quantifying the degree of ordering. Therefore, the distribution of angle deviation can be plotted by shifting the maximum of the Gaussian to 0° (Figure 2B). In the case of wrinkled substrates, the applied shift equals the rotational offset of the wrinkle orientation in the SEM images, which means that AgNWs are predominantly oriented parallel to the wrinkles.

A 2D nematic order parameter S_{2D} can be classically calculated from the distribution of the angular deviation relative to a reference orientation α_{ref}:

$$S_{2D} = \langle 2\,cos^2(\alpha - \alpha_{ref}) - 1 \rangle \qquad \textbf{Equation 1}$$

where the brackets denote the weighted average over the distribution of angular deviation. Note that the 2D nematic order parameter usually reflects the angular deviation from the main orientation direction, i.e. that $\alpha_{ref} = \alpha_{max}$, which results in S_{2D} values between 1 and 0. In the course of this work, we observe the coexistence of AgNWs that are mainly aligned parallel or perpendicular to the wrinkles. Therefore, we decided to systematically define the wrinkle orientation (or the spraying direction for the flat substrate) as the reference orientation α_{ref} independently of the predominant direction of particles and thereby allow negative values of S_{2D}. The sign of the order parameter thus nicely indicates if the main fraction of particles is parallel (positive) or perpendicular (negative) to the wrinkle orientation (Fig. S4). Indeed, $S_{2D} = 0$ corresponds to an isotropic deposition (Fig. S5), whereas $S_{2D} = +1$ represents an ensemble of AgNWs perfectly oriented along the wrinkles ($\alpha = \alpha_{ref}$) and $S_{2D} = -1$ describes AgNWs perfectly oriented perpendicular to the wrinkles ($\alpha = \alpha_{ref} \pm 90°$).

The deposition of AgNWs on a flat substrate with the spraying conditions used here results in a thin film with a nematic order parameter of $S_{2D} = 0.71$, which corresponds to ~50% of AgNWs being oriented within ±15° from the spraying direction. In contrast, spraying under the same conditions on a wrinkled substrate leads to $S_{2D} = 0.94$ (>95% of AgNWs within ±15° from the wrinkle direction). This high degree of orientation is achieved homogenously over $>5 \times 5$ mm^2 area. It must be noted that AgNWs are very well oriented over the wrinkled areas, whereas they are deposited with a lower density and orientation within the cracks (as an example, a crack is visible on the top of the right image of Figure 2A). Although wrinkles represent >90% of the total substrate area, and the cracks only 7 ± 2% (as measured from a statistical analysis of a collection of optical micrographs (Fig. S6)), the few misoriented nanowires deposited in the cracks perpendicular to the wrinkle direction reduce the overall order parameter: indeed, $S_{2D} = 0.94$ when considering the entire population of deposited AgNWs (i.e. including those in the cracks), whereas $S_{2D} = 0.98$ if AgNWs in the wrinkled area only are considered. Such high ordering could be obtained over macroscopic scales if crack-free wrinkled surfaces could be produced, which remains a challenge.[70-73]

AgNWs are preferentially deposited on the top of the wrinkles, although a significant number of AgNWs are also present in the valleys (Fig. S2A). As the wrinkles have a wavelength of ~950 nm, which corresponds to ~20 times the AgNW average diameter, a few AgNWs may fit on each wrinkle crest, and the structure can thus be described as "stripes" of ~400–500 nm width over which 3–5 AgNWs are deposited side-by-side, separated by stripes of approximately the same width with a much lower density of AgNWs corresponding to the wrinkle valleys.

It is thus obvious that the presence of wrinkles enhances the degree of AgNWs ordering when the suspension is sprayed along the wrinkle direction. This brings up the question of the

robustness of such an effect: is the preferential orientation along the substrate corrugations preserved even if the suspension is not sprayed along the wrinkles but at a different angle in the xy-plane, or would the AgNWs rather align along the spraying direction as they do on a flat substrate? In order to answer this question, the angle φ between the spraying and wrinkle directions has been varied, as shown on Figure 1, from φ = 0° (spraying parallel to the wrinkles) to φ = 90° (spraying perpendicular to the wrinkles). Figure 3A shows the color-coded SEM images which were taken a few millimeters away from the point of impact of the spray jet on the surface (as indicated by the red square in the inset) obtained with a spraying angle of φ = 45° and φ = 90°, which can be compared to Figure 2A (φ = 0°).

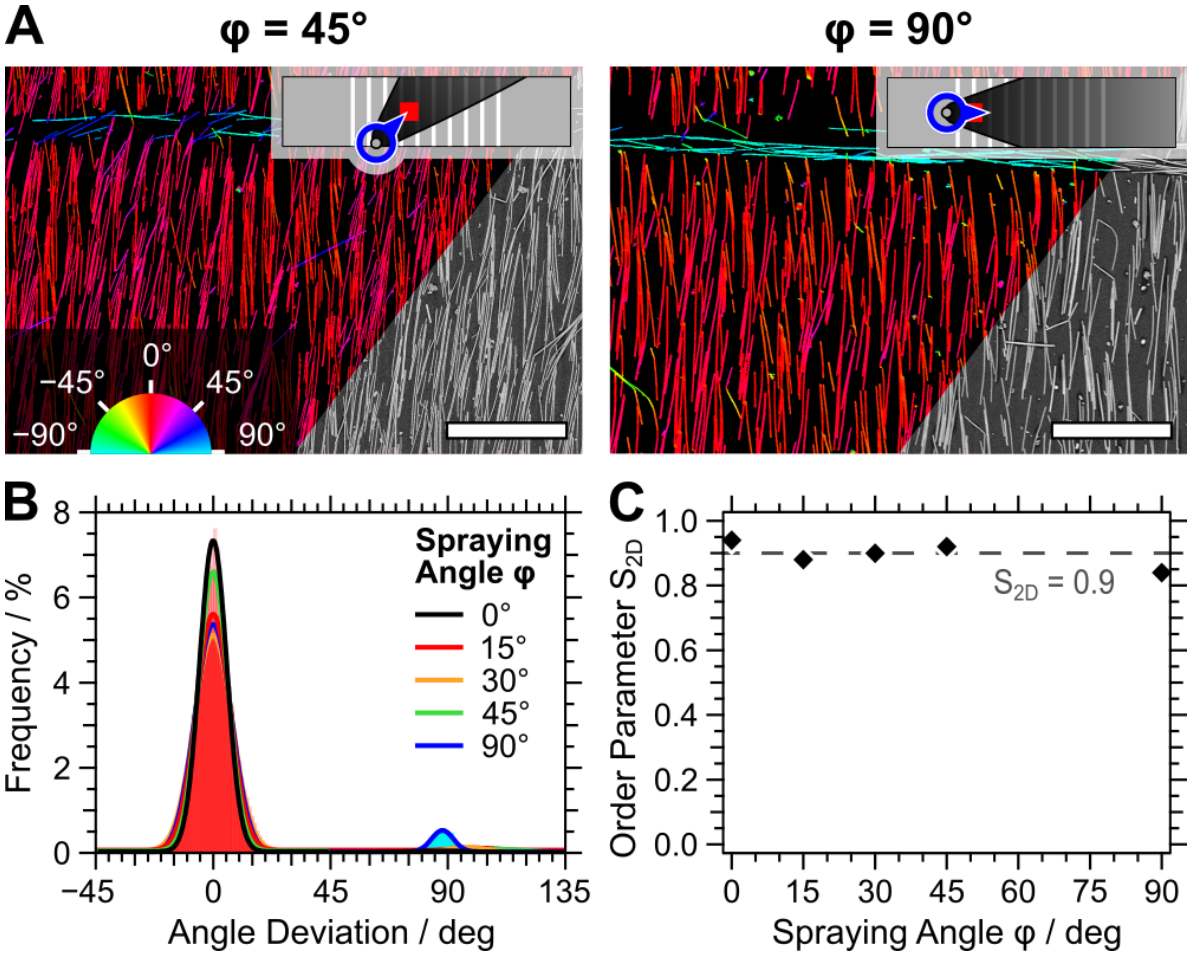

Figure 3. *Systematic study of the alignment at various spraying angle φ between the spray jet*

and the wrinkle direction ($0° \leq \varphi \leq 90°$). (A) Orientation analysis of SEM images sprayed at $\varphi = 45°$ (left) and 90° (right). SEM images are split into the orientation-highlighted and the original images (color scale shown as inset, scale bar 5 µm). The positions at which the images have been taken are highlighted with a red square on the schematic of the samples (inset). (B) Corresponding histograms of the orientations found for each spraying angle. (C) 2D order parameter (S_{2D}) with respect to the spraying angle φ.

Interestingly, AgNWs located close to the impact point are mainly oriented along the wrinkle direction both for $\varphi = 45°$ and $\varphi = 90°$ despite the offset of the spraying direction (Figure 3A). The assembly obtained resembles very much the structure obtained for $\varphi = 0°$ (Figure 2A). However, whereas for $\varphi = 45°$ this wrinkle-dominated alignment is observed over the whole sprayed area (except for the very boundaries), on the sample sprayed at $\varphi = 90°$ this is only true near the impact point, as it will be discussed in details later. In general, AgNWs are mostly deposited in a highly oriented way on top of the wrinkles, whereas less AgNWs are present in the grooves of the wrinkles. The cracks are partially filled with AgNWs that orient along the cracks. However, it appears clearly from the angle deviation distribution (Figure 3B) that the majority of AgNWs are well oriented along the wrinkles ($\alpha = 0°$), and only a minor part is oriented along the cracks direction ($\alpha = 90°$). The average order parameter is thus not very much affected by the spraying angle, and S_{2D} only slightly varies around an average value of 0.91 (Figure 3C).

In a series of previous reports, we have shown that gold nanorods,[57] silver nanowires[57,58] and cellulose microfibrils[59] are all oriented along the spraying direction while spraying at low out-of-plane angle on a flat substrate due to the shear forces exerted by the flowing liquid on those 1D nano-objects. Interestingly, here we find that AgNWs orient along the wrinkle direction even when sprayed perpendicular to the wrinkles ($\varphi = 90°$). This suggests that the corrugations

strongly modify the assembly process: indeed, wrinkles may reorient the liquid flow near the solid-liquid interface, or the substrate-AgNW interaction that favors an adsorption along the wrinkles (larger contact area) may be stronger than the shear forces exerted by the flowing liquid.

However, a careful look at a sample sprayed perpendicularly to the wrinkles ($\varphi = 90°$) reveals that the AgNW orientation is not identical over the entire substrate. The spraying time has been reduced from 250 s to 120 s to decrease the AgNW coverage below saturation. Indeed, AgNW thin films build up following a competitive random sequential adsorption, and the coverage increases quickly within the first tens of seconds before reaching a plateau.[58] A series of 161×121 μm^2 sized SEM panorama images has been taken every ~1 mm starting at the edge of the 2×1 cm^2 wrinkled area (starting position = 0 cm) close to the impact point of the spray jet and moving progressively further away along the central axis of the sample (Fig. 4A insets). Representative images at various locations on the central axis (0, 5 and 12 mm) are given in Figure 4A, together with the angular deviation distribution measured on large-scale images taken at the same positions (Figure 4B).

It appears that AgNWs are nicely oriented along the wrinkle direction (and thus perpendicular to the spraying direction) close to the impact point (left panel), whereas they are aligned along the spraying direction (i.e. perpendicular to wrinkles) far away from the impact point (right panel). In between, there is a transition from AgNWs oriented along wrinkles to AgNWs perpendicular to them that extends over a few millimeters. This transition is imaged over its full length in the supporting Movie S1.

The predominant direction of AgNWs is either along or perpendicular to the wrinkles. Therefore, the transition occurs by a changing ratio of area covered by domains of the two

orientations rather than a gradual change in orientation angle. At ~5 mm (middle panel), the thin film consists of regions of a few hundreds μm^2 containing each a few tens of AgNWs. At this position, the two possible orientations are approximately balanced, and the structure can thus be described as domains of highly oriented AgNWs, approximately half of them being oriented along the wrinkles and the other half along the spraying direction. The angular distribution (Figure 4B) further confirms this observation: the distribution close to the impact point is a narrow Gaussian centered around the wrinkle direction ($\alpha = 0°$), with only a small fraction of AgNWs oriented around $\alpha = 90°$ which corresponds to the few nanowires deposited in the cracks. This narrow orientation distribution results in an average nematic order parameter $S_{2D} = 0.89$. On the contrary, the distribution of angular deviation measured 10 mm further away from the impact point is centered on $\alpha = 90°$ (spraying direction), with almost no nanowire around $\alpha = 0°$, and $S_{2D} = -0.88$. The average nematic order parameter $S_{2D} = -0.15$ at the transition between these two extreme situations is close to zero. Indeed, the distribution of angle deviation clearly shows that the thin film is composed of two populations centered on both perpendicular directions, which individually would yield $S_{2D} \sim +1$ and $S_{2D} \sim -1$, respectively. As both orientation show approximately the same frequency, their order parameters cancel out each other to yield an averaged S_{2D} around zero.

The mapping of the transition from one orientation to the other has been probed by measuring the nematic order parameter S_{2D} on SEM images taken every 1 mm along the central axis of the sample, while moving away from the impact point (Figure 4C, see also Movie S1). The transition occurs between ~2 and ~8 mm away from the edge of the wrinkled area as seen in the decrease of S_{2D} from a value of > 0.8 to < -0.8. A more detailed analysis of the transition is given in Figure S7, which shows that the average AgNW density stays around 60–70% over the first

12 mm, and then smoothly decreases to a very low coverage (~20% at 20 mm). At each position, there are two populations of AgNWs centered around $\alpha = 0°$ and $\alpha = 90°$, each one with a low average angle deviation (5–15°). However, the proportion of each population changes continuously in the transition region from $> 95\%$ of AgNWs oriented around the wrinkle direction close to the impact point to $> 95\%$ of AgNWs oriented around the spraying direction > 8 mm further away from the impact point (see Movie S1).

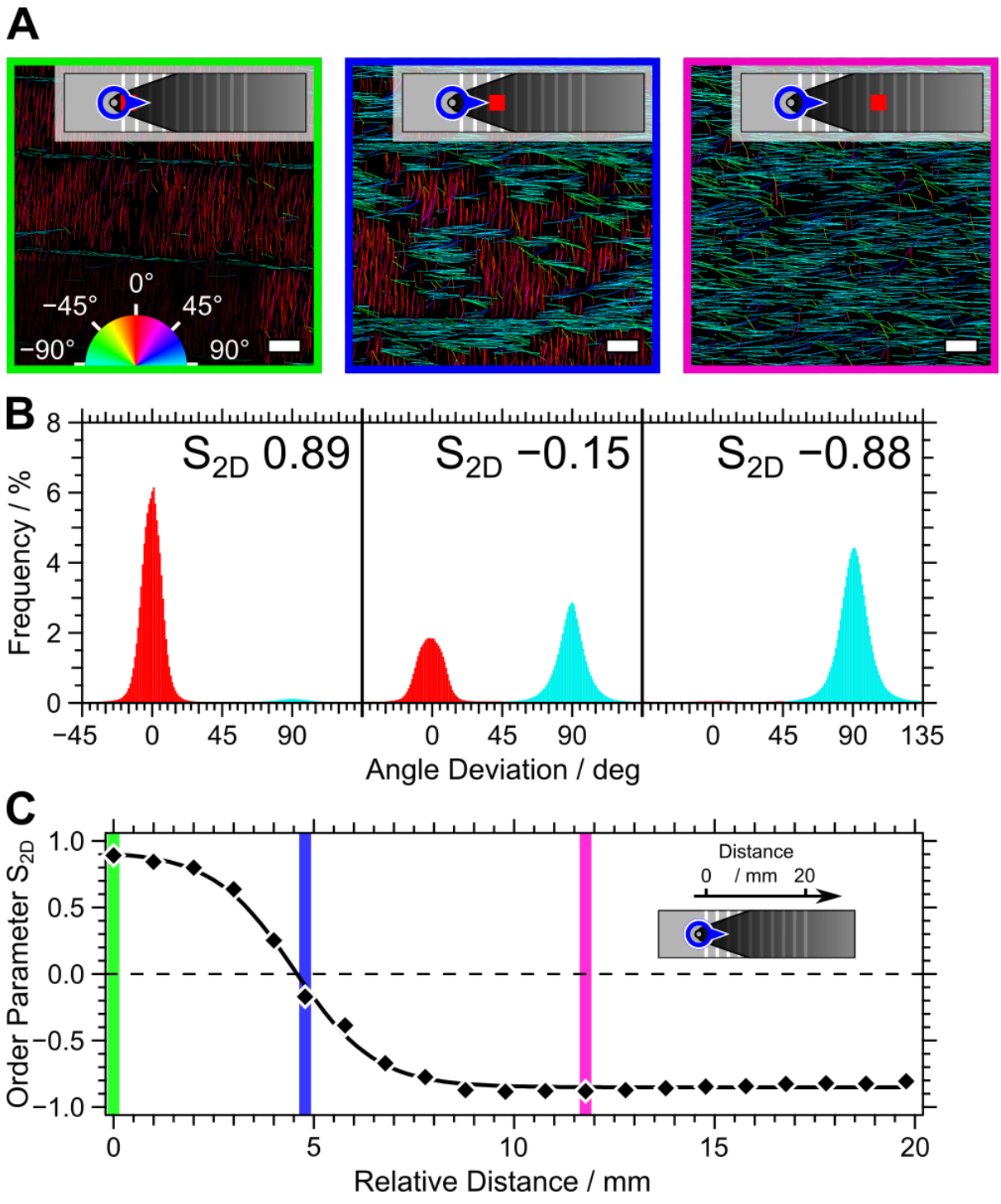

Figure 4. *Detailed position-dependent evaluation of an AgNW oriented thin film sprayed at* $\varphi = 90°$*, the insets show the position of the evaluated area (green squares) on the sprayed parabolic area. (A) Orientation analysis of SEM images (color scale shown as inset, scale bar*

5 µm). (B) Corresponding histograms of the orientations and (C) 2D order parameter S_{2D} with respect to distance from the edge of the wrinkled area. S_{2D} is fitted by a sigmoidal function.

This smooth transition from AgNWs oriented along wrinkles close to the spray jet to AgNWs oriented along the liquid flow further away is counterintuitive: one could expect that the influence of the shear force exerted by the flowing liquid is highest where the velocity is highest, i.e. close to the nozzle, whereas the effect of the substrate is getting dominant while the velocity is reduced far from the spraying nozzle. However, the AgNW orientation that is observed reveals that the influence of wrinkles is higher close to the impact point. The flow and velocity of the AgNW suspension on the substrate is mainly arising from the high gas flow exiting the nozzle (30 L/min). Indeed, the gas exits the nozzle with a high velocity at an out-of-plane angle of 15° with respect to the substrate. While hitting the sample, the gas flow is redirected parallel to the surface, drags away the liquid film already present on the substrate and slows down as the distance from the nozzle increases. Consequently, close to the nozzle the gas velocity comprises two components acting normal and parallel to the substrate. In contrast, the velocity component perpendicular to the substrate is negligible far from the nozzle. This reduces the thickness of the liquid film close to the nozzle, which enhances the relative influence of the substrate. Here, the assembly seems to be governed by capillary forces pushing the particles toward the corrugated surface to promote the topographical confinement effect of the wrinkles. On the contrary, the thickness of the liquid film is larger further away from the spray nozzle, and the influence of its shear force is becoming dominant. Shear-induced orientation of rod-like particles is an old problem[74] and is still an active field of research.[75-78] Furthermore, the balance between shear forces and surface-dominated oriented adsorption is likely to depend on various experimental parameters including gas flow rate, solvent viscosity and spraying time. Therefore, an exact

understanding and quantification of the forces at play would require in-situ monitoring of the nanowire adsorption in real time and modeling of the flow-induced shear forces and substrate-nanowire interaction, which is beyond the scope of the present study.

AgNWs have optical properties that arise from the Localized Surface Plasmon Resonance of the conduction band electrons. The anisotropic shape of individual AgNWs gives rise to several modes that are linked to oscillations of the electrons along the short axis of AgNWs (transverse LSPR modes) and along their long axis (longitudinal LSPR modes). As demonstrated above, the morphological anisotropy at single-particle level is transferred to macroscopic scale by the large-area linear orientation of AgNWs in the thin film induced by GIS. Consequently, the oriented thin film should exhibit anisotropic optical properties on large scales that can be probed by conventional polarized UV-Vis-NIR optical spectroscopy (Figure 5).

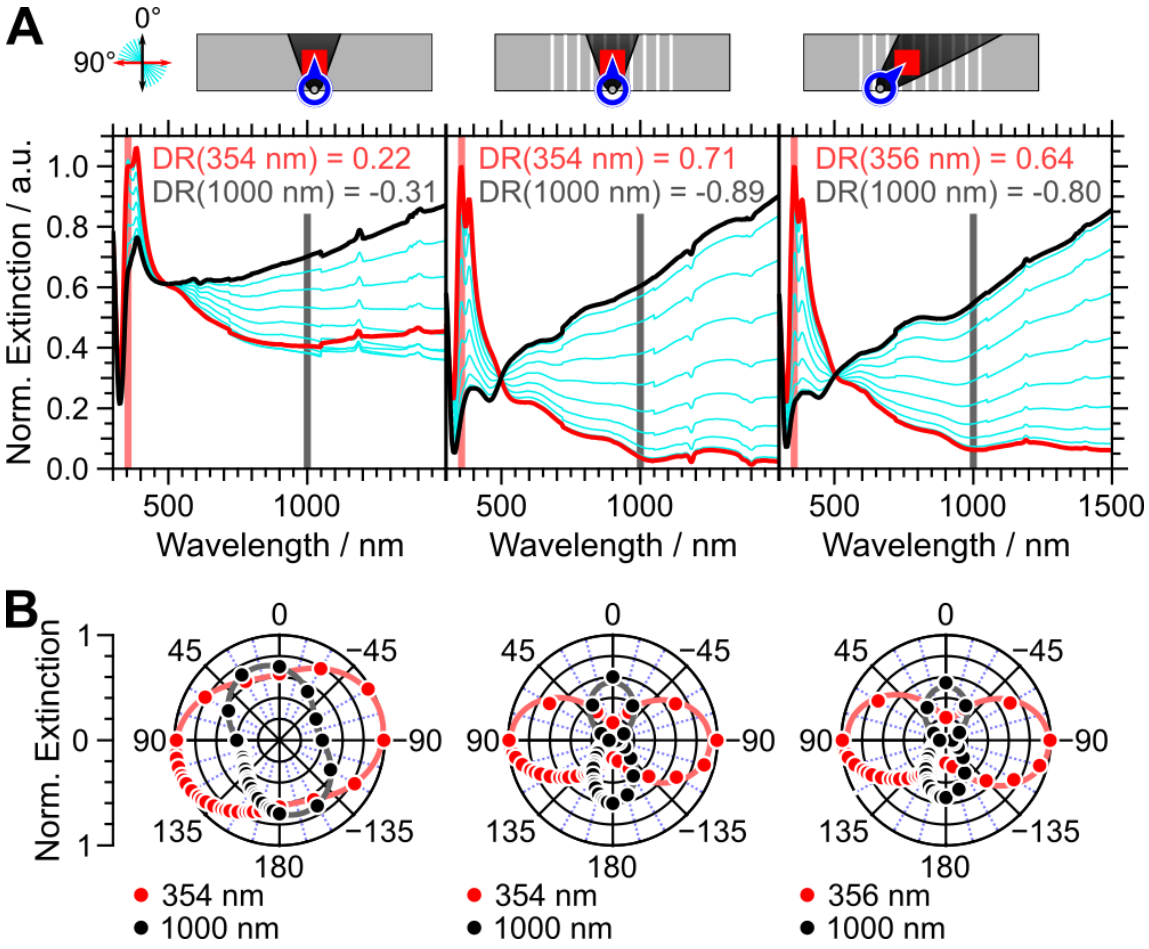

Figure 5 *Optical characterization using polarized UV-Vis-NIR spectroscopy on flat and wrinkled (φ = 0° and 45°) GIS samples. (A) Normalized extinction cross-section of the polarized UV-Vis-NIR spectroscopy evaluated as function of the angle β between the direction of light polarization and the wrinkle direction in 10°-steps, starting from polarization along the wrinkles (β = 0°, black line), intermediate angles (light blue) and ending at perpendicular to the wrinkles (β = 90°, red line). Comparison of the extinction in both directions yields the dichroic ratio (Equation 2) used as a benchmark for the optical anisotropy. (B) Polar plot representation of the normalized extinction cross-section (radius) as function of the polarization angle β for two representative wavelength (354 nm and 1000 nm), which can be correlated to transverse and*

longitudinal resonances, respectively. The solid lines represent sine square and cosine square fits to the measured data.

Polarized UV-Vis-NIR spectra (Figure 5A) have been measured on a macroscopic area (5×5 mm^2) located at the center of the parabolic spray pattern for the samples deposited on a flat substrate and on wrinkled substrates with spraying applied along the wrinkle direction ($\varphi = 0°$) and at $\varphi = 45°$ (the structure of these samples is shown in Figure 2 and Figure 3A, respectively). The angle of light polarization β, defined with respect to the wrinkle direction (or spraying direction in case of flat substrate), has been varied from 0° to 90° in 10° steps. When the incoming light beam is linearly polarized along the wrinkles, and thus along the long axis of AgNWs ($\beta = 0°$, black spectra), the longitudinal modes of the LSPR are selectively excited for all the characterized substrates, which results in a broad band starting at ~500 nm and extending toward the NIR (the maximum of this band is above 2500 nm, the highest wavelength accessible with our spectrometer). On the contrary, when light is polarized along the AgNWs short axis ($\beta = 90°$, red spectra), the LSPR transverse modes are selectively excited, giving rise to two extinction peaks centered at 354–356 nm and at 383 nm. The spectra for $0° < \beta < 90°$ are intermediate to these two extreme situations, and both the transverse and the longitudinal bands are excited to a certain degree depending on the polarization angle β. The polarized spectra clearly show that the transverse and longitudinal modes can be selectively excited on a macroscopic scale depending on the light polarization direction, which is a direct proof of the large-area orientation of AgNWs with a high degree of alignment.

The extinction at a specific wavelength can be measured as function of the polarization angle β and represented in a polar plot. Figure 5B shows the normalized extinction at the low-energy transverse band position (354–356 nm, red dots) and in the longitudinal tail at 1000 nm (black

dots). This polar representation clearly highlights the extinction anisotropy: indeed, the extinction is maximum in the NIR (longitudinal LSPR band) and minimum in the UV (transverse LSPR band) when light is polarized parallel to the wrinkles and thus the AgNW long axis ($\beta = 0°$ and 180°), whereas the extinction is minimum in the NIR and maximum in the UV when light is polarized perpendicular to the wrinkles, i.e. along the AgNW short axis ($\beta = \pm 90°$). The extinction as function of polarizer angle can be nicely fitted with a sine square (transverse LSPR) or cosine square function (longitudinal LSPR). The thin film sprayed on the flat substrate shows a slight angular offset, the maximum extinction of the longitudinal tail being at $\beta \sim 15°$ and not at $\beta = 0°$ as expected. The reason may be that the optical properties have been measured slightly away from the central axis of the parabolic spray pattern. Indeed, the alignment direction of AgNWs gradually shifts away from the central axis while moving towards the edges of the deposited thin film due to the opening of the spray cone.

The normalized difference of the extinction measured with the polarization perpendicular ($\beta = 90°$) and parallel ($\beta = 0°$) to the wrinkle direction gives the dichroic ratio DR that measures the optical anisotropy:

$$DR = \frac{Ext_{\beta=90°} - Ext_{\beta=0°}}{Ext_{\beta=90°} + Ext_{\beta=0°}} \qquad \textbf{Equation 2}$$

Please note that the dichroic ratio is defined (similarly to the nematic order parameter) with respect to the wrinkle orientation and not with respect to the main anisotropy axis as it is usually done in the literature. Consequently, the dichroic ratio, as defined in Eq. 2, can take negative values and the sign of DR describes the predominant orientation of the AgNWs: when AgNWs are oriented along the wrinkles, DR is positive for the transverse LSPR band ($Ext_{\beta=90°} > Ext_{\beta=0°}$), whereas DR is negative for the longitudinal LSPR tail ($Ext_{\beta=90°} < Ext_{\beta=0°}$). The sign of DR is reversed for AgNWs oriented perpendicular to the wrinkles.

The absolute value of DR is clearly linked to the degree of ordering of the AgNWs, as evidenced (Table 1) by the correlation between the dichroic ratio (optical anisotropy) and the nematic order parameter (morphological anisotropy). Indeed, the less ordered thin film sprayed on the flat substrate ($S_{2D} = 0.71$) has a DR = 0.22 at 354 nm and DR = –0.31 at 1000 nm, whereas the more ordered film sprayed on wrinkles at $\varphi = 0°$ ($S_{2D} = 0.94$) displays a DR = 0.71 at 354 nm and DR = –0.89 at 1000 nm. These values are very close to the theoretical maximum of DR modeled by finite-difference time-domain (FDTD) simulations ($DR_{theo}(354\ nm) = 0.82$, $DR_{theo}(1000\ nm) = –0.98$, see Fig. S8), which stresses the high quality of alignment over macroscopic areas. Indeed, the improved AgNW orientation induced by the wrinkled substrate leads to more pronounced anisotropic optical properties, as evidenced by the increased DR. Furthermore, the sample sprayed at $\varphi = 45°$ has a DR = 0.64 at 356 nm and DR = –0.80 at 1000 nm which are only few % lower than the values obtained for the sample sprayed along the wrinkles ($\varphi = 0°$). This further demonstrates that wrinkled substrates enhance the robustness of the deposition process by GIS, especially as spraying at an angle of 45° with respect to the wrinkles only leads to a small reduction of the degree of ordering, which reflects in the resulting optical anisotropy. Wrinkles thus have the ability to "correct" the effect of local inhomogeneities of the flow or of variations in the spraying angle due to the opening of the spray cone for instance.

Table 1. Nematic order parameters S_{2D} and dichroic ratios DR of oriented AgNW thin films measured for the transverse localized surface plasmon resonance (T-LSPR) and at the longitudinal tail at 1000 nm. Please note that the optical properties and the SEM images have been made on different samples. Furthermore, the S_{2D} values given here are an average over 5

different spots to match the size of the area that is probed during UV-Vis-NIR spectroscopy, which explains the small differences with the S_{2D} values given in the corresponding figures.

Sample		***S_{2D}***	***DR(T-LSPR)***	***DR(1000 nm)***
Flat substrate		0.71	0.22	–0.31
Wrinkled substrate	Sprayed at $\varphi = 0°$	0.94	0.71	–0.89
	Sprayed at $\varphi = 45°$	0.92	0.64	–0.80
	Sprayed at $\varphi = 90°$ (observed close to impact point)	0.68	0.63	–0.33
	Sprayed at $\varphi = 90°$ (observed far from impact)	–0.88	–0.54	0.77
Single AgNW (simulations)		"1.00"	0.82	–0.98

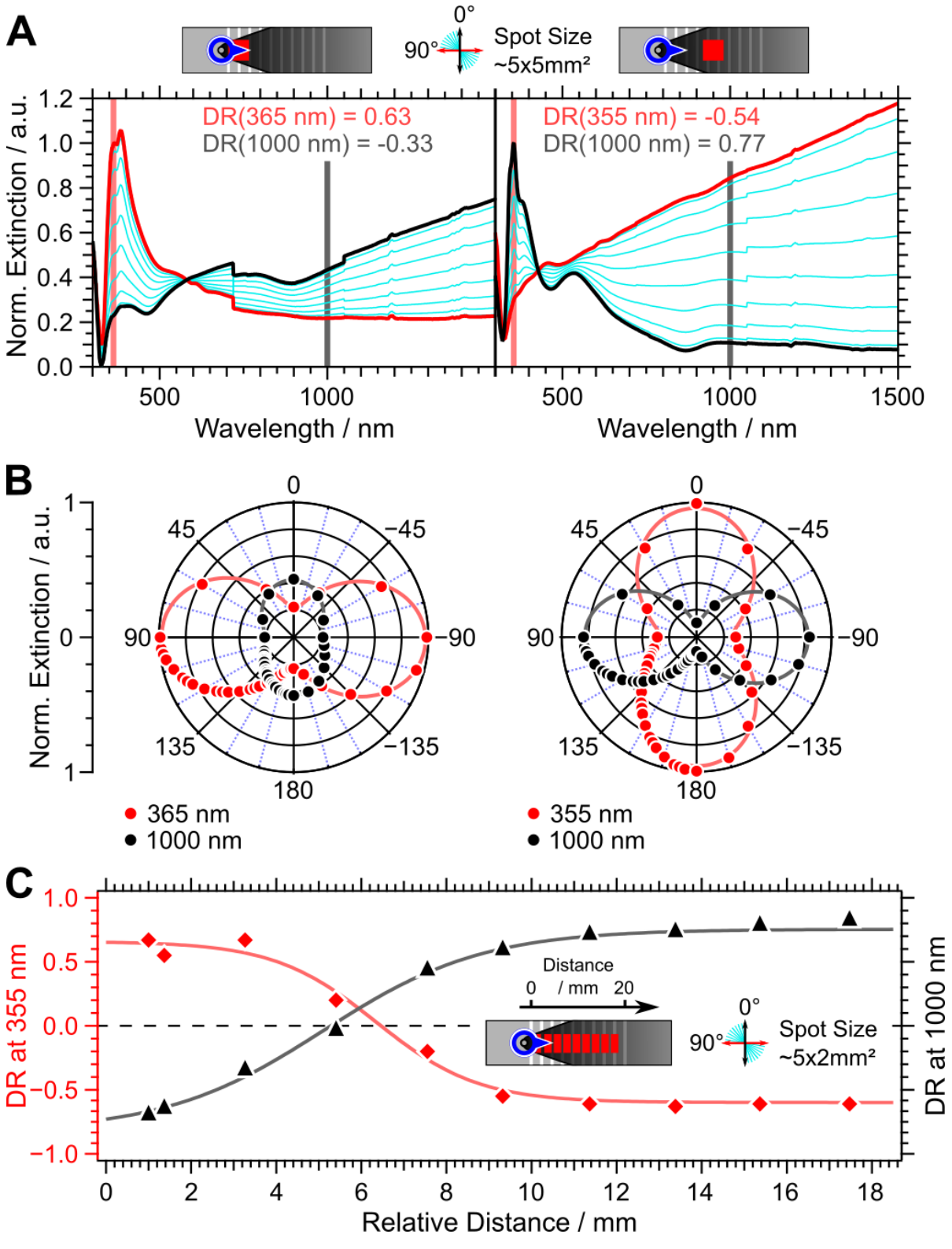
A
0°
90°
Spot Size
~5x5mm²
DR(365 nm) = 0.63
DR(1000 nm) = -0.33
DR(355 nm) = -0.54
DR(1000 nm) = 0.77
Norm. Extinction / a.u.
Wavelength / nm
B
Norm. Extinction / a.u.
365 nm
1000 nm
355 nm
1000 nm
C
DR at 355 nm
DR at 1000 nm
Distance
0 / mm 20
Spot Size
~5x2mm²
Relative Distance / mm

Figure 6. *Detailed optical characterization of the gradually varying orientation of AgNWs sprayed perpendicular to the wrinkles. (A) Normalized extinction cross-section of the polarized UV-Vis-NIR spectroscopy evaluated as function of the angle β between the direction of light polarization and the wrinkle direction in 10°-steps. The spectra are measured on a macroscopic area (5 × 5 mm²) at two different positions on the same sample (red squares on the sample schematics): close to the edge of the wrinkled area (left panel) and 10 mm away (right panel). Comparison of the extinction with light polarized parallel (black curve) or perpendicular (red curve) to the wrinkle direction yields the dichroic ratio (equation 2) as benchmark for the observed anisotropy and particle orientation. The spectra are normalized with respect to the extinction of the high-energy transverse band. (B) Corresponding polar plots of the normalized extinction as function of the polarization angle β measured for the high-energy transverse mode (red dots) and for the longitudinal tail at 1000 nm (black dots). The lines represent respectively sine square and cosine square fits to the measured data. (C) Detailed mapping of the dichroic ratio at 355 nm (red diamonds) and at 1000 nm (black triangles) on 5 × 2 mm² spots separated by 2 mm, which highlights the gradual transition of the average particle orientation with increasing distance from the impact point of the spray. The error bars display the uncertainty that arises due to the degradation of the plasmonic particles with measuring time.*

The optical properties of the thin film sprayed at $\varphi = 90°$ are presented in Figure 6. Figure 6A shows the spectra measured as function of the angle β between light polarization and the wrinkle direction on a 5 × 5 mm² spot at two different positions on the thin film. AgNWs are oriented along the wrinkles close to the impact point of the spray jet (Figure 4A), and the spectra (left panel) thus resemble the ones measured for $\varphi = 0°$ (Figure 5A): the extinction is maximum at the

transverse LSPR band for light polarized perpendicular to the wrinkles. The dichroic ratio DR is equal to 0.63 at 365 nm and to –0.33 at 1000 nm, which is close to the values obtained for $\varphi = 0°$, and which is consistent with the nematic order parameter $S_{2D} = 0.68$ measured at this location. However, as discussed previously (Figure 4), the average AgNW orientation changes gradually when moving away from the impact point of the spray jet from AgNWs oriented along the wrinkles to AgNWs oriented perpendicular to wrinkles. Consequently, the polarized UV-Vis-NIR spectra are reversed 1 cm away from the impact point (Figure 6A, right panel) as compared to the situation near the impact point: the extinction is maximum at the transverse LSPR band for light polarized parallel to the wrinkles and thus perpendicular to the AgNWs long axis. The change of orientation is also obvious from the polar plots (Figure 6B and Movie S2) of the extinction as function of polarization angle β: the polarization angle-dependent variation in extinction of the transverse LSPR band (355–365 nm, red dots) close to the impact point of the spray jet has a similar shape but is perpendicular to the extinction measured far away from the impact point.

In order to map the transition from one preferred orientation to the other, UV-Vis-NIR spectra have been measured on 2×5 mm^2 spots every 1 mm along the sample central axis. The corresponding dichroic ratios at 355 nm and 1000 nm are given in Figure 6C. Close to the impact point of the spray jet, the dichroic ratio at the transverse (355 nm) and longitudinal (1000 nm) LSPR bands are DR = 0.67 and DR = –0.69 respectively, which is expected for AgNWs oriented along the wrinkles with a high degree of ordering. Consistently with the smooth transition from one orientation to the other described in Figure 4, the DR of the transverse LSPR band decreases from 0.70 to –0.70 while moving away from the impact point, while the DR of the longitudinal LSPR tail increases from –0.70 to 0.70 over the same distance. The change of sign of the DR is

characteristic of the change of orientation evidenced by SEM. Both measured DR values are close to zero at a distance of ~6 mm away from edge of the wrinkled area, which is consistent with the fact that the thin film is composed of ~50% of AgNWs oriented parallel and ~50% oriented perpendicular to the wrinkles at this position.

The spectra measured away from the impact point show an additional peak at ~535 nm that is maximum for $\beta = 0°$ and that is almost not visible for $\beta = 90°$. This peak is due to the coupling of the individual transverse LSPR modes of neighboring AgNWs, and this additional coupling peak is only present when the transverse LSPR modes are excited (i.e. for β being close to 0).

Conclusion

In this work, we have shown that the oriented deposition of AgNWs with Grazing Incidence Spraying on a wrinkled substrate leads to highly oriented monolayer thin films over large areas. While GIS on flat substrates is able to induce orientation of AgNWs over ~1 cm^2, the use of textured substrate enhances the degree of ordering and increases the area over which AgNWs are oriented. The corrugated surface seems to guide the liquid flow. Even when spraying is performed with a certain angular deviation relative to the wrinkle orientation, AgNWs still have a strong tendency to be aligned along the wrinkles rather than in the direction of the liquid flow. The consequence is an increased robustness of the oriented deposition process: even if the spray is not perfectly parallel to the wrinkles (which typically happens on the edges of the spray pattern), the direction of orientation is dominated by the wrinkles. Such a large-area orientation of AgNWs leads to thin films that have anisotropic optical properties at a macroscopic scale.

Finally, the high versatility of the proposed approach must be highlighted. Indeed, GIS has been shown to be efficient to orient a broad range of 1D-nanomaterials, including gold nanorods, carbon nanotubes, and cellulose microfibrils,[57-59] and although some differences will exist for objects having a different size and a different surface chemistry, the same wrinkle-assisted spray-induced orientation approach can in theory be used for any type of nanowire or nanorod. Even for low aspect ratio nanorods (AR ~6), wrinkled substrates can significantly enhance the linear alignment. As depicted in Fig. S9, we found an increase in the order parameter from $S_{2D} = 0.28$ (flat PDMS) to $S_{2D} = 0.65$ for spraying along the wrinkles. Similarly to AgNWs, the transverse (~ 530 nm) and longitudinal bands (~ 1080–1110 nm) can be selectively excited, leading to an increased optical anisotropy for the wrinkled substrate. Indeed, the dichroic ratio measured for the longitudinal mode increases from –0.18 for the flat substrate to –0.41 for the wrinkled one. Optimizing the wavelength and depth of the wrinkles should even enable a better linear alignment.

Furthermore, the density of deposited nano-objects can be very easily tuned by varying the spraying time and the concentration of the suspension, which will modify the optical properties of the resulting thin film. It must also be noted that such nanoparticle structures deposited on wrinkled substrates can be transferred[49] to flat substrates in order to be integrated into more complex devices that may comprise several layers of different materials.

The counterintuitive observation that the orientation of AgNWs can be changed from one direction to its perpendicular one on the same substrate by spraying at 90° from the wrinkle direction highlights the concomitant influence of substrate-governed adsorption that favors the alignment along the wrinkles and of spray-induced shear forces that favor orientation along the spraying direction. The transition from one orientation to the other on the same sample highlights

that a subtle balance between shear forces and substrate-nanowire interactions mediated by wrinkles offers a new way to control the self-assembly of nanoparticles into more complex patterns. Furthermore, we found out that the nanowires adsorbed in the cracks of the PDMS substrate are oriented in the perpendicular direction compared to AgNWs on the wrinkled part, and patterning of the surface with "controlled cracks", made for instance by selective etching, could lead to thin films in which selected areas on the same substrate could have different orientations.

Experimental section

Chemicals

Poly(ethyleneimine) (PEI, $\overline{M_n} \approx 60{,}000$ g/mol), poly(vinylpyrrolidone) (PVP, $\overline{M_w} \approx 40{,}000$ g/mol), silver nitrate and glycerol were purchased from Sigma-Aldrich (France). Sodium chloride was purchased from Carl Roth GmbH (Germany). Sylgard 184 Polydimethylsiloxane (PDMS) kit was supplied by Dow Corning (USA). All chemicals were used without further purification. Aqueous solutions were prepared with ultrapure water (resistivity = 18.2 MΩ.cm, Milli-Q Gradient system, Millipore, France).

Synthesis of Silver Nanowires (AgNWs)

Silver nanowires were synthesized by a polyol reduction procedure previously reported in the literature.[7,58] 1.76 g of PVP were dissolved into 57 mL of glycerol kept at 90°C under stirring till a homogeneous solution was obtained. After cooling down to room temperature, 0.47 g of $AgNO_3$ was added, followed by a NaCl solution consisting of 17.7 mg of NaCl dissolved in 0.15 mL of ultrapure water and 3 mL of glycerol. The solution was heated in 20 minutes from room temperature to 210°C, after what heating was stopped, 60 mL of ultrapure water were

added and the solution was left to cool down to room temperature. The precipitate at the bottom of the flask was collected after having left the flask undisturbed for one week. The obtained AgNWs were washed 10–15 times with Milli-Q water by centrifugation at 2000 rpm for 30 minutes, and finally suspended in 170 mL of water (concentration: 1.20 mg/mL, as determined by freeze-drying and weighing a known of volume of AgNW suspension). The synthesized AgNWs have a cross section of 47 ± 6 nm and a length of 4.2 ± 1.5 μm, as determined by Transmission Electron Microscopy (TEM).

Wrinkle preparation

PDMS was prepared by mixing 25 g of the commercially available prepolymer, which consists in a linear dimethylsiloxane oligomer (n~60) with vinyl end groups for crosslinking by hydrosilylation, and the cross-linker at a ratio of 10:1 (by weight) in a rectangular polystyrene dish. The mixture was degassed in a desiccator in vacuum to remove all air bubbles. The cross-linking step is made at room temperature by leaving the covered plastic dish on a leveled plate overnight to ensure a homogeneous thickness of the PDMS slab. Subsequently, it was annealed at 80 °C for 5 h to ensure full cross-linking. Next, the cross-linked elastomer was cut into pieces 1×4 cm^2 in size, and stretched along their long axis to a strain of 30–40% using a homemade stretching device. The stretched PDMS substrate was subjected to a 0.2 mbar oxygen plasma treatment (Flecto 10, operated at 100% plasma power, Plasma Technology, Germany) for 950–1200 s. Aforementioned variations in strain and plasma exposure duration were necessary to compensate for changes in ambient humidity that affect the resulting wrinkle geometry. Upon exposure to O_2 plasma, the surface of PDMS oxidizes into a stiff SiO_2-like thin layer. Relaxing the substrate provokes a buckling instability due to the mechanical mismatch between the bulk elastic substrate and the uppermost stiff thin layer to induce the formation of wrinkles

perpendicular to the stretching direction. The wrinkle topography can be described analogously to a sine function characterized by its wrinkle periodicity (λ) and amplitude (A). The averaged values determined by atomic force microscopy (AFM, Dimension 3100 NanoScope IIIa and V, Bruker, USA) measured in tapping mode using stiff cantilevers (40 N/m, 300 kHz, Tap300, BudgetSensors, Bulgaria) were $\lambda = 950 \pm 20$ nm and $A = 130 \pm 10$ nm. In addition to the wrinkles, some wider cracks extending along the stretching direction are formed caused by the stress in the brittle layer induced by lateral expansion of the substrate upon relaxation.

The wrinkled PDMS substrates were attached to a glass slide to avoid bending of the flexible PDMS substrates during spray coating. To this end, the glass substrates were cleaned by ultra-sonication in water for 10 min followed by copious rinsing with ethanol and drying under N_2 stream. Subsequently, they were treated for 2 min with air plasma (PDC-002, Harrick Plasma, USA) simultaneously with the wrinkled-PDMS substrate turned upside down (i.e. with the non-wrinkled side facing the plasma). Both plasma-activated surfaces (glass and PDMS) were brought into close contact and let at rest for at least 15 min to securely cross-link the wrinkled elastomeric PDMS slab onto the rigid glass substrate.

AgNWs oriented deposition by Grazing Incidence Spray (GIS)

Prior to AgNW deposition, the wrinkled substrates bound to glass slides were plasma activated for 2 min and subsequently coated with a PEI anchoring layer deposited by spraying an aqueous PEI solution (2.5 mg/mL) for 20 s followed by water-rinsing for 10 s using air-pump spray cans (Roth, France). AgNWs were deposited by Grazing Incidence Spraying (GIS),[57-59] using a homemade spraying setup equipped with 2-fluid nozzles (internal diameter: 300 μm, Spraying Systems, USA) for 250 s unless otherwise specified (air flow 30 L/min, liquid flow 1 mL/min).

The out-of-plane angle between the central axis of the cone of the spray jet and the receiving substrate was fixed at $\theta = 15°$ (Figure 1B), and the nozzle and substrate were held at a constant distance of 1 cm. The so-called spraying angle φ, defined as the in-plane angle between the 2D projection of the spraying direction and the wrinkle orientation (Figure 1B) was varied from 0° (parallel to the wrinkles) to 90° (perpendicular to the wrinkles).

Electron Microscopy and characterization of orientation

The procedure for SEM images treatment and orientation analysis is detailed in the Supporting Information in the Fig. S2, S3 and S4. The samples were imaged by Scanning Electron Microscopy employing a NEON 40 FIB-SEM workstation (Carl Zeiss Microscopy GmbH, Oberkochen, Germany) operated at 1 kV. As dense AgNW thin films provide enough conductivity to reduce charging effects to a minimum, no metal sputtering was applied to preserve the optical properties for subsequent UV-Vis-NIR spectroscopy measurements.

For the orientation analysis, usually $38 \times 26\ \mu m^2$ images were evaluated (2048 × 1374 px, pixel size 18.6 nm). Comparison of order parameters at different spots on the sample ensured sufficient statistical reliability, and more than 1000 particles are analyzed on each image. The SEM-mapping (Fig. 4) was done using SEM panorama images ($161 \times 121\ \mu m^2$, 8640 × 6480 px, pixel size 18.6 nm). This allowed to capture a ~20 times larger area with the same high resolution to ensure statistical significance. The software TrakEM2,[79] a plugin to ImageJ,[68,69] was used to perform the stitching of these 5 × 5 sub-images panoramas.

In order to gain information on the AgNW alignment itself, the wrinkle structure was partially filtered out during data acquisition (Fig. S2): all images for orientation analysis were captured using the Energy Selective Backscattered (ESB) electron detector with ESB grid voltage set to 900 V. Due to the superior scattering cross section of silver, AgNWs appear bright in the image,

whereas the wrinkle structure nearly vanishes completely. To further remove the wrinkles and spherical silver impurities from the image, a threshold was applied using Yen's method[80] in ImageJ and spherical pixel clusters with circularity above 0.5 were filtered out by the particle analysis feature. The resulting image only displays AgNWs and spherical impurities in contact with AgNWs and therefore could not be detected as being spherical.

The orientation of the "filtered" SEM images was evaluated using OrientationJ,[67] a plugin for ImageJ.[68,69] This macro is based on the analysis of the structure tensor of the gray-level in a local neighborhood. Briefly, it determines the local orientation for each pixel of the SEM image and attributes a color corresponding to the angle of orientation α (Fig. S2 and S3). A Gaussian window of 3 px (comparable to the AgNW diameter) was applied for the OrientationJ analysis. A histogram of orientations is extracted from the resulting false color image. Here, pixels with coherency below 5 % and/or energy below 1 % were ignored.

Further evaluation of these distributions of orientation found in SEM was done in Igor Pro (Wavemetrics, USA) to finally retrieve the nematic order parameter S_{2D} (Fig. S4). Usually particles are preferably aligned vertical in the SEM images (parallel to the wrinkles), which corresponds to an angle α of 0°. Shifting the maximum of the Gaussian distribution in x-direction to exactly 0° yields the angular deviation from the predominant orientation. As the angular shift equals the rotational offset of the wrinkles in the SEM images, the predominant direction is parallel to the wrinkles. By applying Eq.1, the angle deviation values can be translated into S_{2D} values. The normalized distribution is used as weighing to calculate the averaged order parameter. The consistency of this evaluation was cross-checked on random arrangements of AgNWs dropcasted on flat, PEI-coated PDMS (Fig. S5). Here the evaluation

yielded $S_{2D} = 0.05$, which is close to zero and therefore agrees well with a random distribution of orientations.

In the case of the mapped sample with gradually varying preferred orientation of AgNWs (Fig. 4), there are regions far away from the impact point where nearly no particles are aligned parallel to the wrinkles. As the reference orientation for the calculation of S_{2D} should remain the wrinkling orientation nonetheless, the evaluation of the angle distributions had to be slightly modified. The maximum of the Gaussian distribution representing particles perpendicular to the wrinkles (parallel to the spraying) was shifted to 90° of angle deviation. This indirectly locates the wrinkle orientation at zero to enable the aforementioned calculation of the order parameter with wrinkle orientation as reference orientation. This is only valid if both particle orientations are perfectly perpendicular to each other. By studying SEM images having large amounts of particles of both orientations this could be verified, though: shifting of AgNWs parallel to wrinkles to 0° and shifting of AgNWs perpendicular to wrinkles to 90° yields the same results for S_{2D} (Fig. S4 + Table S1).

The coverage of the substrate with AgNWs was calculated as the ratio of the number of detected AgNW pixels to the amount of pixels within the analyzed SEM image.

UV-Vis-NIR spectroscopy

UV-Vis-NIR spectroscopy was measured in transmission geometry using a Cary 5000 spectrophotometer (Agilent, USA) equipped with the Universal Measurement Accessory (UMA) and a linear polarizer. The spot size on the sample was approx. 5×5 mm^2 for all measurements except for the mapping presented in Fig. 4 which was measured with a spot size of 5×2 mm^2. The measured extinction is corrected from the contribution of a blank wrinkled PDMS substrate

taken as a reference. The polarizer can be rotated to vary the angle between the light polarization plane and the oriented AgNWs. The polarization direction (polarization angle β) is defined with respect to the wrinkle direction (i.e. $\beta = 0°$ when light is polarized along the wrinkles and $\beta = 90°$ when it is perpendicular to the wrinkle direction).

ASSOCIATED CONTENT

Supporting Information. The Supporting Information includes two movies showing the transition from one orientation to the other on the sample described in Fig. 4 (Movie S1) and the change in the corresponding optical properties (Movie S2). It also includes a PDF file which contains AFM height images of flat and wrinkled PDMS substrates (Fig. S1), the detailed procedure used for SEM processing and orientation analysis (Fig. S2), the orientation analysis of a model image (Fig. S3), the detailed procedure for the evaluation of the AgNW orientation (Fig. S4), the analysis of a drop-casted AgNW sample showing no orientation (Fig. S5), a large scale optical micrograph used to evaluate the crack density (Fig. S6), a detailed analysis of the SEM mapping of the sample described in Fig. 4 (Fig. S7), the FDTD simulation of the extinction spectra as function of polarization angle (Fig. S8), SEM images and polarized spectra of gold nanorods sprayed on a wrinkled substrate (Fig. S9) and a Table comparing the S_{2D} values obtained following two different evaluation procedures. The following files are available free of charge.

AUTHOR INFORMATION

Corresponding Author

* decher@unistra.fr, fery@ipfdd.de, matthias.pauly@ics-cnrs.unistra.fr

Author Contributions

‡ P. P. and S. S. contributed equally to this work.

ACKNOWLEDGMENT

This study was partially funded by the European Research Council under grant ERC-2012-StG 306686 (METAMECH: Template assisted assembly of METAmaterials using MECHanical instabilities). This work was also supported by the Deutsche Forschungsgemeinschaft (DFG) within the Cluster of Excellence 'Center for Advancing Electronics Dresden' (cfaed). P.T.P. appreciates the support of the Elite Network Bavaria (ENB) in the framework of the Elite Study Program "Macromolecular Science". M.P. acknowledges the IDEX program of the University of Strasbourg and the joint "Chaire d'Excellence" program of CNRS/University of Strasbourg for partial funding. G.D. thanks the Institut Universitaire de France (IUF) for financial support. The authors acknowledge Jean Farago (ICS, Strasbourg, France) for fruitful discussions.

REFERENCES

1. Liu, Z.; Xu, J.; Chen, D.; Shen, G. Flexible electronics based on inorganic nanowires. *Chem. Soc. Rev.* **2015**, *44*, 161-192.
2. Lee, H.; Kim, I.; Kim, M.; Lee, H. Moving beyond flexible to stretchable conductive electrodes using metal nanowires and graphenes. *Nanoscale* **2016**, *8*, 1789-1822.
3. Kang, S.; Kim, T.; Cho, S.; Lee, Y.; Choe, A.; Walker, B.; Ko, S.-J.; Kim, J. Y.; Ko, H. Capillary Printing of Highly Aligned Silver Nanowire Transparent Electrodes for High-Performance Optoelectronic Devices. *Nano Lett.* **2015**, *15*, 7933-7942.
4. Wu, F.; Li, Z.; Ye, F.; Zhao, X.; Zhang, T.; Yang, X. Aligned silver nanowires as transparent conductive electrodes for flexible optoelectronic devices. *J. Mater. Chem. C* **2016**, *4*, 11074-11080.
5. Wang, J.; Gudiksen, M. S.; Duan, X.; Cui, Y.; Lieber, C. M. Highly Polarized Photoluminescence and Photodetection from Single Indium Phosphide Nanowires. *Science* **2001**, *293*, 1455-1457.
6. Boehm, S. J.; Kang, L.; Werner, D. H.; Keating, C. D. Field-Switchable Broadband Polarizer Based on Reconfigurable Nanowire Assemblies. *Adv. Funct. Mater.* **2017,** *27,* 1604703.
7. Liu, J.-W.; Wang, J.-L.; Huang, W.-R.; Yu, L.; Ren, X.-F.; Wen, W.-C.; Yu, S.-H. Ordering Ag nanowire arrays by a glass capillary: A portable, reusable and durable SERS substrate. *Sci. Rep.* **2012**, *2*, 987.
8. Ma, W.; Xu, L.; Wang, L.; Kuang, H.; Xu, C. Orientational nanoparticle assemblies and biosensors. *Biosens. Bioelectron.* **2016**, *79*, 220-236.
9. Soukoulis, C. M.; Wegener, M. Past achievements and future challenges in the development of three-dimensional photonic metamaterials. *Nat. Photonics* **2011**, *5*, 523-530.
10. Meinzer, N.; Barnes, W. L.; Hooper, I. R. Plasmonic meta-atoms and metasurfaces. *Nat. Photonics* **2014**, *8*, 889-898.
11. Ackermann, T.; Neuhaus, R.; Roth, S. The effect of rod orientation on electrical anisotropy in silver nanowire networks for ultra-transparent electrodes. *Sci. Rep.* **2016**, *6*, 34289.
12. Boles, M. A.; Engel, M.; Talapin, D. V. Self-Assembly of Colloidal Nanocrystals: From Intricate Structures to Functional Materials. *Chem. Rev.* **2016,** *116,* 11220-11289.
13. Zuojia, W.; Feng, C.; Thomas, W.; Yongmin, L. Optical chiral metamaterials: a review of the fundamentals, fabrication methods and applications. *Nanotechnol.* **2016**, *27*, 412001.
14. Yu, N.; Genevet, P.; Kats, M. A.; Aieta, F.; Tetienne, J.-P.; Capasso, F.; Gaburro, Z. Light Propagation with Phase Discontinuities: Generalized Laws of Reflection and Refraction. *Science* **2011**, *334*, 333.
15. Mühlig, S.; Cunningham, A.; Dintinger, J.; Scharf, T.; Bürgi, T.; Lederer, F.; Rockstuhl, C., Self-assembled plasmonic metamaterials. In *Nanophotonics*, 2013; Vol. 2, p 211.
16. Liu, N.; Guo, H.; Fu, L.; Kaiser, S.; Schweizer, H.; Giessen, H. Three-dimensional photonic metamaterials at optical frequencies. *Nat. Mater.* **2008**, *7*, 31-37.
17. Kildishev, A. V.; Boltasseva, A.; Shalaev, V. M. Planar Photonics with Metasurfaces. *Science* **2013**, *339,* 1232009.
18. Minovich, A. E.; Miroshnichenko, A. E.; Bykov, A. Y.; Murzina, T. V.; Neshev, D. N.; Kivshar, Y. S. Functional and nonlinear optical metasurfaces. *Laser Photonics Rev.* **2015**, *9*, 195-213.

19. Yu, N.; Capasso, F. Flat optics with designer metasurfaces. *Nat. Mater.* **2014**, *13*, 139-150.
20. Yao, K.; Liu, Y. Plasmonic metamaterials. *Nanotechnol. Rev.* **2014**, *3*, 177-210.
21. Gansel, J. K.; Thiel, M.; Rill, M. S.; Decker, M.; Bade, K.; Saile, V.; von Freymann, G.; Linden, S.; Wegener, M. Gold Helix Photonic Metamaterial as Broadband Circular Polarizer. *Science* **2009**, *325*, 1513-1515.
22. Ergin, T.; Stenger, N.; Brenner, P.; Pendry, J. B.; Wegener, M. Three-Dimensional Invisibility Cloak at Optical Wavelengths. *Science* **2010**, *328*, 337-339.
23. Zhao, Y.; Belkin, M. A.; Alù, A. Twisted optical metamaterials for planarized ultrathin broadband circular polarizers. *Nat. Commun.* **2012**, *3*, 870.
24. Zhao, Y.; Shi, J.; Sun, L.; Li, X.; Alù, A. Alignment-Free Three-Dimensional Optical Metamaterials. *Adv. Mater.* **2014**, *26*, 1439-1445.
25. Klinkova, A.; Choueiri, R. M.; Kumacheva, E. Self-assembled plasmonic nanostructures. *Chem. Soc. Rev.* **2014**, *43*, 3976-3991.
26. Jianxiao, G.; Guodong, L.; Zhiyong, T. Self-assembly of noble metal nanocrystals: Fabrication, optical property, and application. *Nano Today* **2012**, *7*, 564 - 585.
27. Gwo, S.; Chen, H.-Y.; Lin, M.-H.; Sun, L.; Li, X. Nanomanipulation and controlled self-assembly of metal nanoparticles and nanocrystals for plasmonics. *Chem. Soc. Rev.* **2016**, *45*, 5672-5716.
28. Boles, M. A.; Engel, M.; Talapin, D. V. Self-Assembly of Colloidal Nanocrystals: From Intricate Structures to Functional Materials. *Chem. Rev.* **2016**, *116*, 11220-11289.
29. Thorkelsson, K.; Bai, P.; Xu, T. Self-assembly and applications of anisotropic nanomaterials: A review. *Nano Today* **2015**, *10*, 48-66.
30. Yan, W.; Xu, L.; Xu, C.; Ma, W.; Kuang, H.; Wang, L.; Kotov, N. A. Self-Assembly of Chiral Nanoparticle Pyramids with Strong R/S Optical Activity. *J. Am. Chem. Soc.* **2012**, *134*, 15114-15121.
31. Hu, T.; Isaacoff, B. P.; Bahng, J. H.; Hao, C.; Zhou, Y.; Zhu, J.; Li, X.; Wang, Z.; Liu, S.; Xu, C.; Biteen, J. S.; Kotov, N. A. Self-Organization of Plasmonic and Excitonic Nanoparticles into Resonant Chiral Supraparticle Assemblies. *Nano Lett.* **2014**, *14*, 6799-6810.
32. Kim, Y.; Yeom, B.; Arteaga, O.; Jo Yoo, S.; Lee, S.-G.; Kim, J.-G.; Kotov, N. A. Reconfigurable chiroptical nanocomposites with chirality transfer from the macro- to the nanoscale. *Nat. Mater.* **2016**, *15*, 461-468.
33. Feng, W.; Kim, J.-Y.; Wang, X.; Calcaterra, H. A.; Qu, Z.; Meshi, L.; Kotov, N. A. Assembly of mesoscale helices with near-unity enantiomeric excess and light-matter interactions for chiral semiconductors. *Science Advances* **2017**, *3,* e1601159.
34. Chen, Z.; Lan, X.; Chiu, Y.-C.; Lu, X.; Ni, W.; Gao, H.; Wang, Q. Strong Chiroptical Activities in Gold Nanorod Dimers Assembled Using DNA Origami Templates. *ACS Photonics* **2015**, *2*, 392-397.
35. Yang, S.; Ni, X.; Yin, X.; Kante, B.; Zhang, P.; Zhu, J.; Wang, Y.; Zhang, X. Feedback-driven self-assembly of symmetry-breaking optical metamaterials in solution. *Nature Nanotech.* **2014**, *9*, 1002-1006.
36. Kuzyk, A.; Schreiber, R.; Zhang, H.; Govorov, A. O.; Liedl, T.; Liu, N. Reconfigurable 3D plasmonic metamolecules. *Nat. Mater.* **2014**, *13*, 862-866.
37. Liu, J.-W.; Liang, H.-W.; Yu, S.-H. Macroscopic-Scale Assembled Nanowire Thin Films and Their Functionalities. *Chem. Rev.* **2012**, *112*, 4770-4799.

38. Kwiat, M.; Cohen, S.; Pevzner, A.; Patolsky, F. Large-scale ordered 1D-nanomaterials arrays: Assembly or not? *Nano Today* **2013**, *8*, 677-694.
39. Long, Y.-Z.; Yu, M.; Sun, B.; Gu, C.-Z.; Fan, Z. Recent advances in large-scale assembly of semiconducting inorganic nanowires and nanofibers for electronics, sensors and photovoltaics. *Chem. Soc. Rev.* **2012**, *41*, 4560-4580.
40. Tao, A. R.; Huang, J.; Yang, P. Langmuir-Blodgettry of Nanocrystals and Nanowires. *Acc. Chem. Res.* **2008**, *41*, 1662-1673.
41. Chen, M.; Phang, I. Y.; Lee, M. R.; Yang, J. K. W.; Ling, X. Y. Layer-By-Layer Assembly of Ag Nanowires into 3D Woodpile-like Structures to Achieve High Density "Hot Spots" for Surface-Enhanced Raman Scattering. *Langmuir* **2013**, *29*, 7061-7069.
42. Hangarter, C. M.; Myung, N. V. Magnetic Alignment of Nanowires. *Chem. Mater.* **2005**, *17*, 1320-1324.
43. Raychaudhuri, S.; Dayeh, S. A.; Wang, D.; Yu, E. T. Precise Semiconductor Nanowire Placement Through Dielectrophoresis. *Nano Lett.* **2009**, *9*, 2260-2266.
44. Trotsenko, O.; Tokarev, A.; Gruzd, A.; Enright, T.; Minko, S. Magnetic field assisted assembly of highly ordered percolated nanostructures and their application for transparent conductive thin films. *Nanoscale* **2015**, *7*, 7155-7161.
45. Huang, Y.; Duan, X.; Wei, Q.; Lieber, C. M. Directed Assembly of One-Dimensional Nanostructures into Functional Networks. *Science* **2001**, *291*, 630-633.
46. Håkansson, K. M. O.; Fall, A. B.; Lundell, F.; Yu, S.; Krywka, C.; Roth, S. V.; Santoro, G.; Kvick, M.; Prahl Wittberg, L.; Wågberg, L.; Söderberg, L. D. Hydrodynamic alignment and assembly of nanofibrils resulting in strong cellulose filaments. *Nat. Commun.* **2014**, *5*, 4018.
47. Assad, O.; Leshansky, A. M.; Wang, B.; Stelzner, T.; Christiansen, S.; Haick, H. Spray-Coating Route for Highly Aligned and Large-Scale Arrays of Nanowires. *ACS Nano* **2012**, *6*, 4702-4712.
48. Efimenko, K.; Rackaitis, M.; Manias, E.; Vaziri, A.; Mahadevan, L.; Genzer, J. Nested self-similar wrinkling patterns in skins. *Nat. Mater.* **2005**, *4*, 293-297.
49. Hanske, C.; Müller, M. B.; Bieber, V.; Tebbe, M.; Jessl, S.; Wittemann, A.; Fery, A. The Role of Substrate Wettability in Nanoparticle Transfer from Wrinkled Elastomers: Fundamentals and Application toward Hierarchical Patterning. *Langmuir* **2012**, *28*, 16745-16750.
50. Hanske, C.; Tebbe, M.; Kuttner, C.; Bieber, V.; Tsukruk, V. V.; Chanana, M.; König, T. A. F.; Fery, A. Strongly Coupled Plasmonic Modes on Macroscopic Areas via Template-Assisted Colloidal Self-Assembly. *Nano Lett.* **2014**, *14*, 6863-6871.
51. Tebbe, M.; Mayer, M.; Glatz, B. A.; Hanske, C.; Probst, P. T.; Muller, M. B.; Karg, M.; Chanana, M.; Konig, T. A. F.; Kuttner, C.; Fery, A. Optically anisotropic substrates via wrinkle-assisted convective assembly of gold nanorods on macroscopic areas. *Faraday Discuss.* **2015**, *181*, 243-260.
52. Mayer, M.; Tebbe, M.; Kuttner, C.; Schnepf, M. J.; Konig, T. A. F.; Fery, A. Template-assisted colloidal self-assembly of macroscopic magnetic metasurfaces. *Faraday Discuss.* **2016**, *191*, 159-176.
53. Volynskii, A. L.; Bazhenov, S.; Lebedeva, O. V.; Bakeev, N. F. Mechanical buckling instability of thin coatings deposited on soft polymer substrates. *J. Mater. Sci.* **2000**, *35*, 547-554.
54. Huang, R.; Suo, Z. Wrinkling of a compressed elastic film on a viscous layer. *J. Appl. Phys.* **2002**, *91*, 1135-1142.

55. Cerda, E.; Mahadevan, L. Geometry and Physics of Wrinkling. *Phys. Rev. Lett.* **2003**, *90*, 074302.
56. Huang, Z. Y.; Hong, W.; Suo, Z. Nonlinear analyses of wrinkles in a film bonded to a compliant substrate. *J. Mech. Phys. Solids* **2005**, *53*, 2101-2118.
57. Sekar, S.; Lemaire, V.; Hu, H.; Decher, G.; Pauly, M. Anisotropic optical and conductive properties of oriented 1D-nanoparticle thin films made by spray-assisted self-assembly. *Faraday Discuss.* **2016**, *191*, 373-389.
58. Hu, H.; Pauly, M.; Felix, O.; Decher, G. Spray-assisted alignment of Layer-by-Layer assembled silver nanowires: a general approach for the preparation of highly anisotropic nano-composite films. *Nanoscale* **2017**, *9*, 1307-1314.
59. Blell, R.; Lin, X.; Lindström, T.; Ankerfors, M.; Pauly, M.; Felix, O.; Decher, G. Generating in-Plane Orientational Order in Multilayer Films Prepared by Spray-Assisted Layer-by-Layer Assembly. *ACS Nano* **2017**, *11*, 84-94.
60. Decher, G. Fuzzy Nanoassemblies: Toward Layered Polymeric Multicomposites. *Science* **1997**, *277*, 1232-1237.
61. Seyrek, E.; Decher, G., Layer-by-Layer Assembly of Multifunctional Hybrid Materials and Nanoscale Devices. In *Polymer Science: A Comprehensive Reference*, Matyjaszewski, K.; Möller, M., Eds. Elsevier: Amsterdam, 2012; Vol. 7, pp 159-185.
62. Richardson, J. J.; Björnmalm, M.; Caruso, F. Technology-driven layer-by-layer assembly of nanofilms. *Science* **2015**, *348*, aaa2491.
63. Richardson, J. J.; Cui, J.; Björnmalm, M.; Braunger, J. A.; Ejima, H.; Caruso, F. Innovation in Layer-by-Layer Assembly. *Chem. Rev.* **2016**, *116*, 14828-14867.
64. Li, Y.; John, J.; Kolewe, K. W.; Schiffman, J. D.; Carter, K. R. Scaling Up Nature: Large Area Flexible Biomimetic Surfaces. *ACS Appl. Mater. Interfaces* **2015**, *7*, 23439-23444.
65. Wang, X.; Tian, W.; Liao, M.; Bando, Y.; Golberg, D. Recent advances in solution-processed inorganic nanofilm photodetectors. *Chem. Soc. Rev.* **2014**, *43*, 1400-1422.
66. Chen, G.; Liang, B.; Liu, Z.; Yu, G.; Xie, X.; Luo, T.; Xie, Z.; Chen, D.; Zhu, M.-Q.; Shen, G. High performance rigid and flexible visible-light photodetectors based on aligned X(In, Ga)P nanowire arrays. *J. Mater. Chem. C* **2014**, *2*, 1270-1277.
67. Rezakhaniha, R.; Agianniotis, A.; Schrauwen, J. T. C.; Griffa, A.; Sage, D.; Bouten, C. V. C.; Vosse, F. N.; Unser, M.; Stergiopulos, N. Experimental investigation of collagen waviness and orientation in the arterial adventitia using confocal laser scanning microscopy. *Biomech. Model. Mechanobiol.* **2012**, *11*, 461-473.
68. Schneider, C. A.; Rasband, W. S.; Eliceiri, K. W. NIH Image to ImageJ: 25 years of image analysis. *Nat. Meth.* **2012**, *9*, 671-675.
69. Abramoff, M. D.; Magalhaes, P. J.; Ram, S. J. Image processing with ImageJ. *Biophotonics International* **2004**, *11*, 36-42.
70. Watanabe, M.; Mizukami, K. Well-Ordered Wrinkling Patterns on Chemically Oxidized Poly(dimethylsiloxane) Surfaces. *Macromolecules* **2012**, *45*, 7128-7134.
71. Li, Z.; Zhang, S.; Zhang, P.; Yang, D.; Jin, G.; Ma, H. Surface initiated polymerization from integrated poly(dimethylsiloxane) enables crack-free large area wrinkle formation. *Polym. Adv. Technol.* **2012**, *23*, 1240-1245.
72. Görrn, P.; Wagner, S. Topographies of plasma-hardened surfaces of poly(dimethylsiloxane). *J. Appl. Phys.* **2010**, *108*, 093522.
73. Xuan, Y.; Guo, X.; Cui, Y.; Yuan, C.; Ge, H.; Cui, B.; Chen, Y. Crack-free controlled wrinkling of a bilayer film with a gradient interface. *Soft Matter* **2012**, *8*, 9603-9609.

74. Thirumalai, D. Effect of elongational flow on the isotropic–nematic phase transition in rod-like systems. *J. Chem. Phys.* **1986**, *84*, 5869-5873.
75. Löwen, H. Colloidal dispersions in external fields: recent developments. *J. Phys.: Condens. Matter* **2008**, *20*, 404201.
76. Leahy, B. D.; Koch, D. L.; Cohen, I. The effect of shear flow on the rotational diffusion of a single axisymmetric particle. *J. Fluid Mech.* **2015**, *772*, 42-79.
77. Rodrigo, L.-F.; Sabine, H. L. K. Binary mixtures of rod-like colloids under shear: microscopically-based equilibrium theory and order-parameter dynamics. *J. Phys.: Condens. Matter* **2016**, *28*, 244022.
78. Wu, Y.; Jiang, Z.; Zan, X.; Lin, Y.; Wang, Q. Shear flow induced long-range ordering of rod-like viral nanoparticles within hydrogel. *Colloids Surf., B* **2017**, *158*, 620-626.
79. Cardona, A.; Saalfeld, S.; Schindelin, J.; Arganda-Carreras, I.; Preibisch, S.; Longair, M.; Tomancak, P.; Hartenstein, V.; Douglas, R. J. TrakEM2 software for neural circuit reconstruction. *PloS one* **2012**, *7*, e38011.
80. Yen, J.-C.; Chang, F.-J.; Chang, S. A new criterion for automatic multilevel thresholding. *IEEE Trans. Image Process.* **1995**, *4*, 370-378.